PAPER

Check for updates

A nanostructured lateral flow immunoassay strip combined with Au@SiO2 SERS nanotags for multiplex biomarker detection

Geng Zhu,†[abc] Yuanbao Zhan,†[abc] Yu Lu,[abc] Fei Zheng, [ID][d] Yu Wan,[ae] Bing Liu,[f] Xi Yang,[abc] Yanhui Wan,[g] Qingjiang Sun, [ID][a] Jingjie Sha,[d] Yan Huang*[abc] and Xiangwei Zhao [ID] *[abc]

Blood biomarker detection can conveniently and non-invasively realize early diagnosis in asymptomatic people with Alzheimer's disease (AD). However, disease biomarkers have extremely low abundance; therefore, ultrahigh sensitive detection techniques are required, which are still a challenge. This research proposes a nanostructured lateral flow immunoassay strip combined with Au@SiO2 surface-enhanced Raman scattering (SERS) nanotags (nanostructured SERS-LFIA) for rapid and low-cost detection and to improve the sensitivity, replacing the conventional test line (T line) with inverse opal nitrocellulose. The nanostructured SERS-LFIA is used to detect AD biomarkers as a possible application in early diagnosis. Two AD biomarkers, $A\beta_{42}$ and $A\beta_{40}$, encoded by SERS nanotags are simultaneously detected on the same nanostructured T line, with a limit of detection (LOD) of 15.3 and 16.8 fg mL^{-1}, respectively, about 10 times lower than that of SERS-LFIA. The nanostructured SERS-LFIA has great potential in the non-invasive detection of AD biomarkers and early diagnosis.

1. Introduction

Early diagnosis and timely intervention are vital for disease screening and treatment.[1,2] However, existing medical tests cannot meet the rapid and convenient clinical requirements. Point-of-care testing (POCT) is a convenient but inexpensive technology that reduces the analysis and processing time, allowing physicians to take timely actions for optimal patient care,[3,4] which is highly in demand for early diagnosis and treatments.

Among many POCT methods, lateral flow immunoassay (LFIA) is the fastest-growing technology due to its rapid response, simplicity, low cost, and low sample consumption.[5,6] However, its low sensitivity and poor quantification hampers its applications in POCT for disease diagnosis.[7,8] Recently, a highly sensitive LFIA

technique has been proposed based on surface-enhanced Raman scattering (SERS) nanotags with unique advantages of ultra-high sensitivity and multi-target detection, broadening the application of traditional LFIA to multiplex and ultrasensitive detection.[9–11]

The nitrocellulose (NC) membrane in SERS-LFIA greatly impacts the detection performance. Its microporous structure determines the sample expansion speed and the capture antibody immobilization on the T line, ultimately affecting the repeatability, sensitivity, and detection performance.[12] However, irregular porous structures at the micron scale lead to scattering and nonuniform distribution of nanoparticles on its surface, thus, affecting optical signal detection.[13,14]

Therefore, a paper with a micropillar scaffold has been synthesized from off-stoichiometry-thiol–ene (OSTE) by lithography to prepare ordered microstructures, improving the detection performance.[15] Compared with state-of-the-art glass and nitrocellulose substrates, the synthetic paper exhibits a stronger fluorescence and lower limit of detection (LOD) in detecting enrofloxacin in milk. In addition, the synthetic paper provides better reproducibility and needs less immunoreagent. However, the aperture of synthetic paper is about 100 μm, which is too large for SERS-LFIA. Chen *et al.* proposed a vertical flow immunoassay system with anodic aluminum oxide (AAO) and SERS nanotags.[16] In contrast to the NC membrane, the AAO membrane is an ordered porous structure membrane at the nanometer scale. It not only facilitates the possibility of the antibody–antigen interaction but also promotes the coupling of

[a] *State Key Laboratory of Bioelectronics, School of Biological Science and Medical Engineering, Southeast University, Nanjing 210096, China*

[b] *Institute of Biomaterials and Medical Devices, Southeast University, Suzhou 215163, China*

[c] *Southeast University Shenzhen Research Institute, Shenzhen 518000, China*

[d] *Jiangsu Key Laboratory for Design and Manufacture of Micro-Nano Biomedical Instruments, School of Mechanical Engineering, Southeast University, Nanjing, China*

[e] *Jiangsu Simcere Pharmaceutical Co., Ltd, Nanjing 210042, China*

[f] *Nantong Univ, Inst Reprod Med, Med Sch, Nantong 226001, China*

[g] *Department of Health Medicine, General Hospital of Eastern Theater Command, PLA, Nanjing 210002, China*
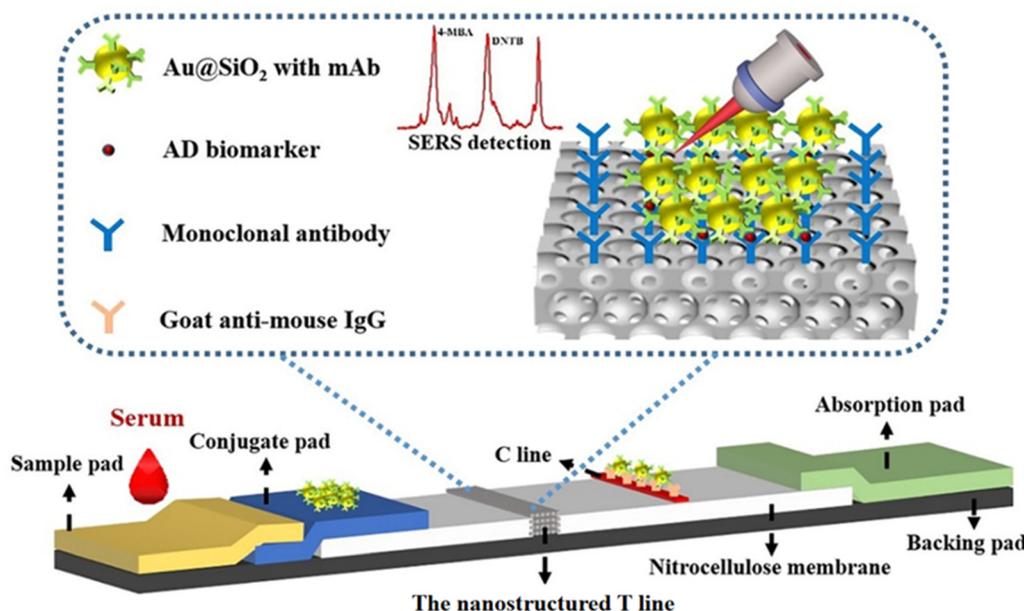
† These authors contributed equally to this work.

Fig. 1 Schematic illustration of multiplex AD biomarker detection by nanostructured SERS-LFIA.

excitation light and plasmonic particles, thus improving the SERS nanotag signals. Therefore, the detection limit for four inflammatory biomarkers reaches the femoral level. Since the fluid can only flow vertically in the AAO membrane, it cannot be used for SERS-LFIA.

Inverse opal nitrocellulose, an ordered micro-nano structure formed by periodic medium arrangement, provides new strategies to overcome these challenges.[17,18] Therefore potential advantages are realized by inverse opal nitrocellulose with SERS-LFIA. First, it interconnects nanopores in the nanoscale, increasing the chance in antigen–antibody interaction by nanoconfinement, thus improving detection sensitivity. Second, the pore sizes are more uniform with a larger surface-to-volume ratio, favored by higher detection performance.

Therefore, in this proof of concept work, an LFIA strip is fabricated with a T line of inverse opal nitrocellulose combined with SERS nanotags and the so-called nanostructured SERS-LFIA for the multiplex detection of biomarkers with ultra-high sensitivity (Fig. 1). Alzheimer's disease (AD) is selected as a model disease to evaluate the nanostructured SERS-LFIAs' performance. When the sample is dropped onto the sample pad and flows laterally to the absorption pad, the biomarkers conjugate with SERS nanotags correspondingly. Then they are captured at the nanostructured T line, where the signal of SERS nanotags quantitatively detects them. Compared with previously reported SERS-LFIA,[19] the nanostructured SERS-LFIA enhances the sensitivity, offering great potential for the early non-invasive detection of AD biomarkers in blood.

2. Experimental section

2.1. Experimental materials and instruments

All reagents were of analytical grade and used without further purification. Nitric acid (HNO_3), hydrochloric acid, tetrachlo-roaurate(III) trihydrate ($HAuCl_4 \cdot 3H_2O$), silver nitrate ($AgNO_3$), trisodium citrate ($Na_3C_6H_5O_7$), bovine serum albumin (BSA), ascorbic acid (AA), ammonia solution, tetraethyl orthosilicate (TEOS), and Tween-20 were purchased from Sinopharm Chemical Reagent Co., Ltd. 3-Glycidyloxypropyltrimethoxysilane (GPTMES), N,N-dimethylformamide (DMF) and 2-hydroxy-1-ethanethiol were supplied by Tianjin C&S Biochemical Technology Co., Ltd. 4-Mercaptobenzoic acid (4-MBA) and 5,5′-dithio bis-(2-nitro-benzoic acid) (DNTB) were obtained from Alfa Aesar. Phosphate buffered saline (PBS) and tri(hydroxymethyl)aminomethane hydrochloride (Tris-HCl) were provided by Sangon Biotech (Shanghai) Co., Ltd.

Human $A\beta_{42}$ peptide, human $A\beta_{40}$ peptide, human tau_{441} protein, a pair of mouse anti-$A\beta_{42}$ monoclonal antibodies, anti-tau monoclonal antibodies, and anti-$A\beta_{40}$ monoclonal antibodies were provided by BioLegend, Inc. Human Neurofilament light chain (NFL) protein and a pair of mouse anti-human NFL antibodies were purchased from Abcam, Inc. Goat anti-mouse IgG antibody was supplied by Beijing Key-Bio Biotech Co., Ltd. The glassware used in these experiments was purchased from Nanjing WANQING chemical Glass ware and Instrument Co., Ltd. Water used to wash glassware and configure reagents was distilled water obtained from the Milli-Q system. All glassware was soaked in a freshly prepared aqua regia solution (HCl/ HNO_3, v/v, 3 : 1) for 2 h and then rinsed thoroughly with distilled water before use. Nylon filters were purchased from Nanjing WANQING chemical Glass ware and Instrument Co., Ltd. Silica particles were obtained from NanJing Nanorainbow Biotechnology Co., Ltd.

Scanning electron microscopy (SEM; Zeiss, Ultra Plus) was used to characterize the morphology of SERS nanotags and inverse opal nitrocellulose. A Raman spectroscopy system (British Renishaw Company) was used to measure the Raman spectra using a 785 nm laser with a power of 3 mW.
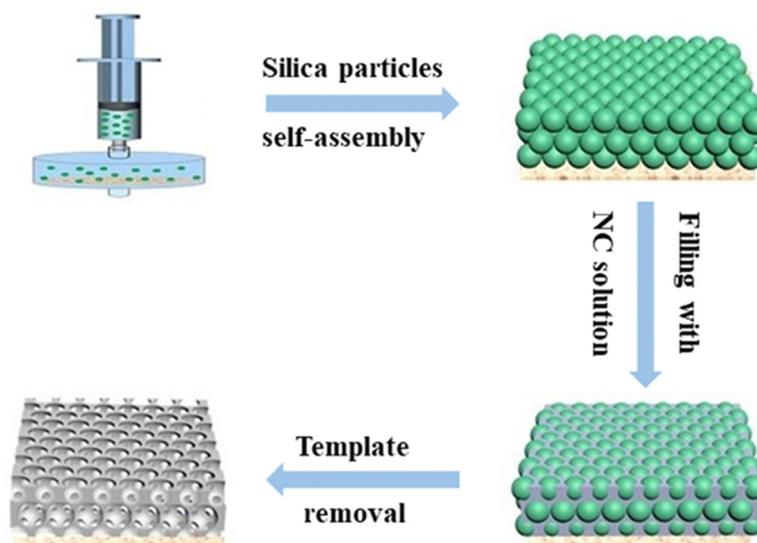
Fig. 2 The fabrication process of inverse opal nitrocellulose.

A 20× objective lens was selected, and the integration time was 10 s.

2.2. Preparation of bio-functioned SERS nanotags

GPTMES functionalized $Au^{4\text{-}MBA}@SiO_2$ and $Au^{DNTB}@SiO_2$ were prepared using a previously reported method.[19] The conjugation of SERS nanotags and antibodies was done as follows: first, the above 1 mL GPTMES functionalized $Au^{4\text{-}MBA}@SiO_2$ and $Au^{DNTB}@SiO_2$ SERS nanotags were mixed with 50 μL of 0.5 mg mL^{-1} $A\beta_{42}$ and $A\beta_{40}$ antibodies, respectively, and incubated for 3 h. The unbound antibodies were removed by centrifugation. Next, the antibody-conjugated SERS nanotags were redispersed in 1 mL of 5% BSA solution and incubated for another 1.5 h. Finally, the blocking solution was removed, and bio-functioned $Au@SiO_2$ SERS nanotags were redissolved in 100 μL of re-suspending solution.

2.3. Fabrication of inverse opal nitrocellulose

Fig. 2 illustrates the fabrication process of the inverse opal nitrocellulose. First, silica particles were purified by centrifugation for 10 min to homogenize the particles. After purification, silica particles were dispersed in ethanol to obtain a 30% (m/v) colloidal solution, filtered vertically onto the nylon filter through a syringe, and self-assembled at room temperature. After 2 h, a self-assembly template with structural color was obtained. An NC solution was prepared by dissolving NC in acetone, and DMF (1 : 1, v/v) mixture and then slowly dripped onto the self-assembly template. After curing for 3 h, the NC membrane containing silica nanoparticles was carefully removed from the nylon filter with distilled water and immersed in a 4% HF solution to etch silica nanoparticles.

2.4. Preparation of the nanostructured SERS-LFIA strip

First, the goat anti-mouse IgG antibody (1 mg mL^{-1}) was anchored on the C line of the NC membrane, dried at 37 °C for 1 h, and stored under a dry atmosphere. Bio-functioned SERS nanotags assigned to the conjugate pad, and dried and stored at room temperature.

The NC membrane was first attached to the middle of the backing pad to fabricate the strip. Second, the inverse opal nitrocellulose was embedded between the NC membrane to replace the conventional T line, and a nanostructured SERS-LFIA strip was completed. Third, $A\beta_{42}$ capturing antibody solution (1 mg mL^{-1}) and $A\beta_{40}$ capturing antibody solution (1 mg mL^{-1}) were mixed and fixed on a nanostructured T line. Next, the absorption, sample, and conjugated pads were fixed to the corresponding position on the backing pad. Finally, the assembled card was cut into 3 mm-wide strips and stored at room temperature for further use.

2.5. Detection of AD biomarkers

The mixtures of $A\beta_{42}$ and $A\beta_{40}$ (1 : 1, v/v) of different concentrations (100 fg mL^{-1} to 10 μg mL^{-1}) were prepared. Then bio-functioned $Au^{4\text{-}MBA}@SiO_2$ SERS and bio-functioned $Au^{DNTB}@SiO_2$ SERS nanotags were used to detect $A\beta_{42}$ and $A\beta_{40}$, respectively. A nanostructured SERS-LFIA was constructed to detect $A\beta_{42}$ and $A\beta_{40}$ simultaneously. 100 μL $A\beta$ solutions of different concentrations were pipetted on the sample pad. After 20 min, the naked eye could observe the color change in nanostructured T and C lines. The appearance of a red band on the C line validated the detection results. A SERS-LFIA was constructed to detect $A\beta_{42}$ in the same way. The Raman signal intensity at 1079 cm^{-1} and 1330 cm^{-1} was then used for the quantitative analysis of $A\beta_{42}$ and $A\beta_{40}$, respectively. Each concentration gradient was tested three times.

3. Results and discussion

3.1. Principal of the nanostructured SERS-LFIA

The schematic of the nanostructured SERS-LFIA was shown in Fig. 1. It comprises five parts: sample pad, conjugate pad, NC membrane, absorbent pad and adhesive backing. It is

remarkable that the traditional T line is replaced by the inverse opal nitrocellulose. The inverse opal nitrocellulose has the following advantages: first, an ordered nanoscale structure can reduce the roughness of the membrane, which is beneficial for the dispersion of detection reagents. Second, the pore size of the inverse opal nitrocellulose can be changed to improve the coupling efficiency between excitation light and SERS nanotags. Third, inverse opal nitrocellulose with appropriate pore size can be selected to improve detection sensitivity. The inverse opal nitrocellulose is prepared by assembly and etching, which has the advantages of simple preparation and adjustable pore size.

3.2. Optimization of inverse opal nitrocellulose

Inverse opal nitrocellulose is affected by the following three factors: nitrocellulose solution concentration, hydrofluoric acid etching time and the diameter of silica particles. In order to achieve highly sensitive AD detection, we optimized three factors separately.

3.2.1. Optimization of nitrocellulose solution concentration.
The concentration of NC solution influences the successful synthesis during the preparation of the inverse opal nitrocellulose. NC solutions of 10%, 7%, 4%, and 1% (w/w) are infused on self-assembled silica particle templates, and morphologies are characterized by SEM. Fig. 3 shows that the NC solutions of 10% and 7% (w/w) are too thick to penetrate the gaps of self-assembled templates of silica particles effectively but form a thick membrane on the surface (Fig. 3a and b), leading to incomplete etching of silica particles by HF solution,

thus preventing the synthesis of inverse opal nitrocellulose. The NC solution of 1% (w/w) is too thin to fill the gaps in silica particles (Fig. 3d); therefore, a complete pore structure might not be obtained by etching with HF solution. Only the 4% (w/w) NC solution effectively penetrates and fills the gaps in silica particles (Fig. 3c), and inverse opal nitrocellulose is obtained after etching with HF solution. Therefore, a 4% NC solution is selected in the subsequent experiments to prepare the ordered NC membranes.

3.2.2. Optimization of hydrofluoric acid etching time.
The etching time of the HF solution also influences the inverse opal nitrocellulose. Therefore, 4% HF etched the self-assembled templates of silica particles filled with NC solution for 3 h, 6 h, 12 h, and 24 h, respectively, and the inverse opal nitrocellulose obtained after SEM characterized etching. After etching for 3 h and 6 h, the self-assembled templates of silica particles are not etched completely (Fig. 4a and b); hence, the inverse opal nitrocellulose is not formed. After being etched for 24 h, the membrane structure is destroyed, although the silica particles are completely etched from the self-assembly template (Fig. 4d). Only after 12 h the silica particles are completely etched without damaging the membrane structure (Fig. 4c), and inverse opal nitrocellulose with smooth and uniform pores is obtained. Therefore, the self-assembled template of silica particles with drip-filled NC solution is etched with 4% HF solution for 12 h in subsequent experiments.

3.2.3. Preparation and selection of the inverse opal nitrocellulose.
Theoretically, preparing the inverse opal nitrocellulose with various pore sizes is feasible by choosing silica
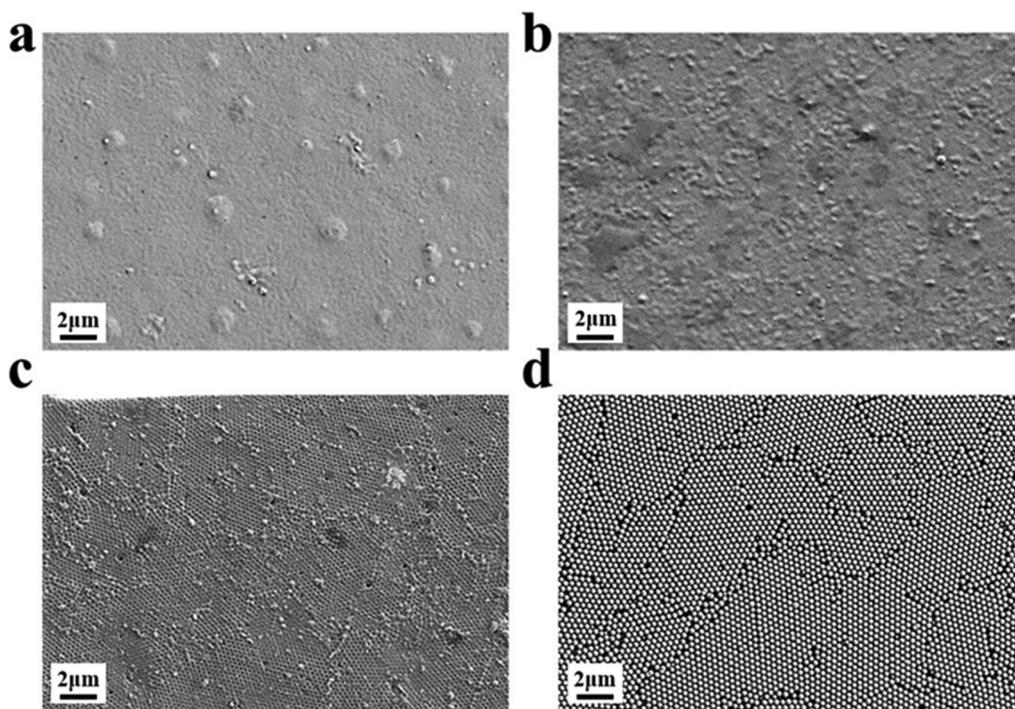

Fig. 3 SEM images of NC solutions with different concentrations infused on self-assembled templates: (a) 10% (w/w), (b) 7% (w/w), (c) 4% (w/w), and (d) 1% (w/w).
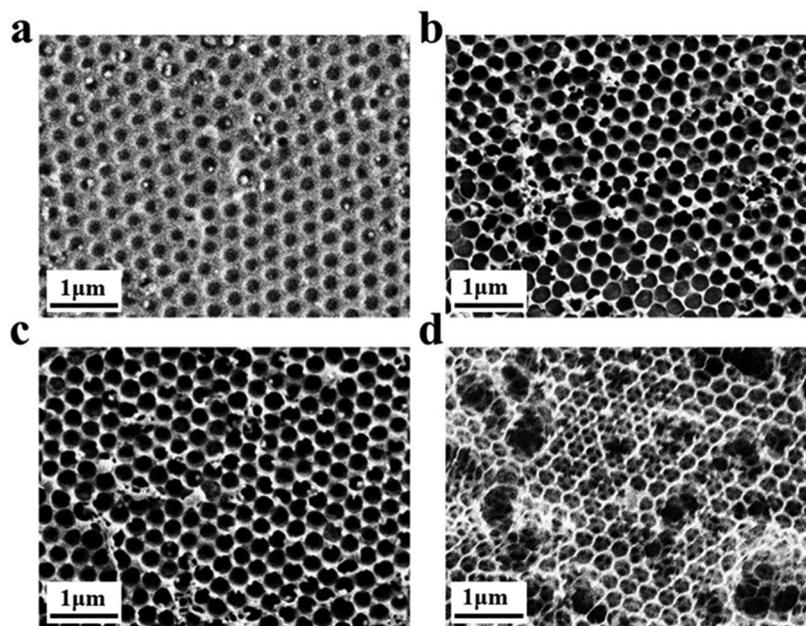
Fig. 4 SEM images of inverse opal nitrocellulose obtained after etching with 4% HF solution for different times: (a) 3 h, (b) 6 h, (c) 12 h, and (d) 24 h.

particles of different sizes.[20–22] However, the diameter of silica particles is limited by two factors. On the one hand, when the diameter of silica particles is more than 400 nm, it cannot be self-assembled to form inverse opal nitrocellulose because a non covalent bond cannot combine particles to form an ordered structure.[23–26] On the other hand, the diameter of the Au@SiO$_2$ SERS nanotag is 80 nm, and inverse opal nitrocellulose with a small pore size will hinder the migration of SERS nanotags. Therefore, monodisperse silica particles of 300 nm, 350 nm, and 400 nm are selected and self-assembled into photonic crystals to determine which aperture of inverse opal nitrocellulose can obtain the strongest Raman signal. Then the 4% (w/w) NC solution is infused on the photonic crystals,

followed by etching with 4% HF solution for 12 h. The self-assembled silica particles' template and the inverse opal nitrocellulose are characterized by SEM.

Fig. 5 shows that all three monodisperse silica particles successfully self-assemble into corresponding templates, and the inverse opal nitrocellulose with corresponding pore sizes is prepared finally. These results indicate that different-sized silica particles could fabricate inverse opal nitrocellulose with different pore sizes. Therefore, inverse opal nitrocellulose with pore sizes of 300, 350, and 400 nm are assembled into test strips separately and tested with Aβ$_{42}$ (100 ng mL^{-1}), the Raman signal is enhanced when the diameter increases from 300 nm to 350 nm and is decreased when the diameter
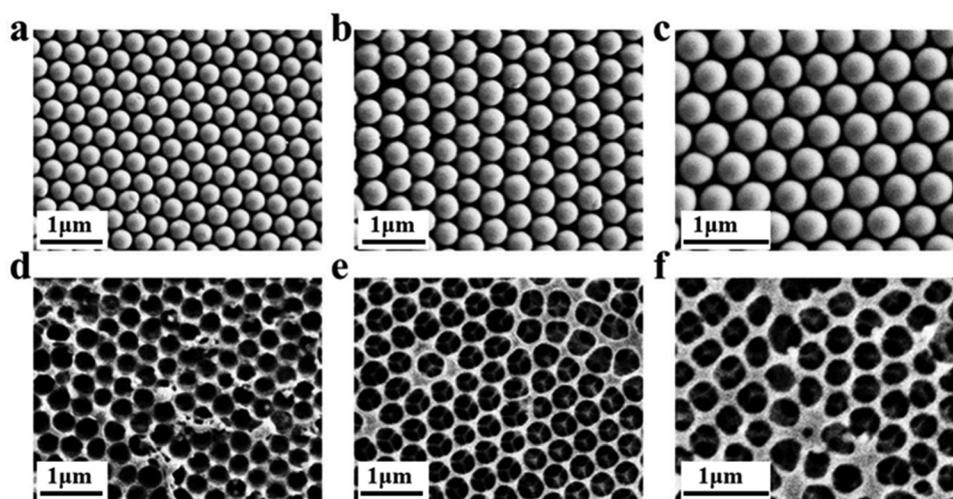

Fig. 5 SEM images of self-assembled templates of monodisperse silica particles with different particle sizes and corresponding inverse opal nitrocellulose. The diameter of silica particles is 300 nm (a) and (d), 350 nm (b) and (e), and 400 nm (c) and (f), respectively.
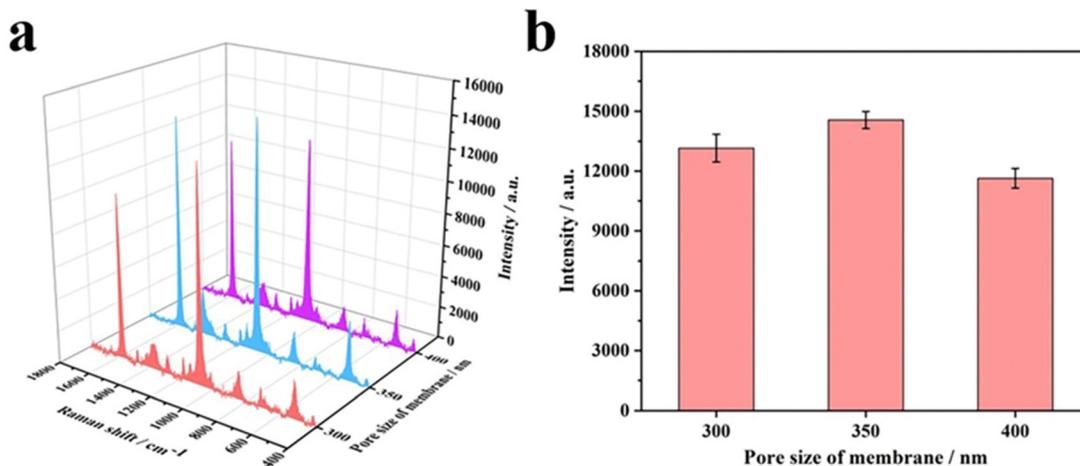
Fig. 6 Raman signals on nanostructured T line with different pore sizes for $A\beta_{42}$ (100 ng mL^{-1}) detections. (a) Raman spectrum; (b) Raman signal intensity at 1079 cm^{-1}. The error bars represent the average of three measurements.

increases to 400 nm (Fig. 6). This phenomenon might be attributed to two reasons: First, the self-assembly effectiveness of monodisperse silica particles with large particle size is not as good as that of small particle size, resulting in an irregular pore size of nanostructured T line. Second, the larger pore size creates a relatively lower specific surface area, which is not conducive to the immune reaction. Therefore, the number of SERS nanotags on a nanostructured T line with a pore diameter of 400 nm is less than that of 350 nm, and the Raman signal is weakened. Therefore, the nanostructured T line with an aperture of 350 nm is selected for subsequent experiments.

3.3. Comparison of nanostructured T line with conventional T line

Firstly, the morphology of the nanostructured T line (350 nm) and the conventional T line is characterized by SEM. The conventional T line has an irregular porous structure at the micron level (Fig. 7a), leading to strong scattering, affecting the optical signals, and preventing homogeneous nanoparticle distribution on its surface. Inversely, the nanostructured T line overcomes these defects (Fig. 7b) and shows nano-confinement effects to favor immune reactions.

According to previous reports, the low flow rate of fluid in the NC membrane is conducive to antigens and antibodies binding.[27] Peristaltic flow in the COMSOL Multiphysics package is applied to simulate the fluid flow rate in the nanostructured and conventional T lines. Fig. 8(a) and (d) show schematic diagrams of the conventional T line and nanostructured T line, respectively. During simulation, the conventional T line is modeled as a rectangular cube with alternately stacked holes of different diameters (3.5, 4, 4.5, and 6 μm). The nanostructured T line is modeled as a rectangular cube with a hexagonal tightly spaced hole, and the diameter of each hole is set to 350 nm. Boundary conditions: no-slip boundary conditions are set on the walls. Laminar flow with a mean velocity of 0.0003 m s^{-1} is set at the inlet, and zero pressure is set at the outlet. Fig. 8(b) and (e) show the flow velocity in the longitudinal-section of the conventional T line and nanostructured T line, respectively. Fig. 8(c) and (f) show the flow velocity in the cross-section of the conventional T line and nanostructured T line, respectively. Compared with the conventional T line, liquid travels slower to prevent more reactant delivery within a certain time in the nanostructured T line, which leads to highly efficient and uniform immune binding, meanwhile a
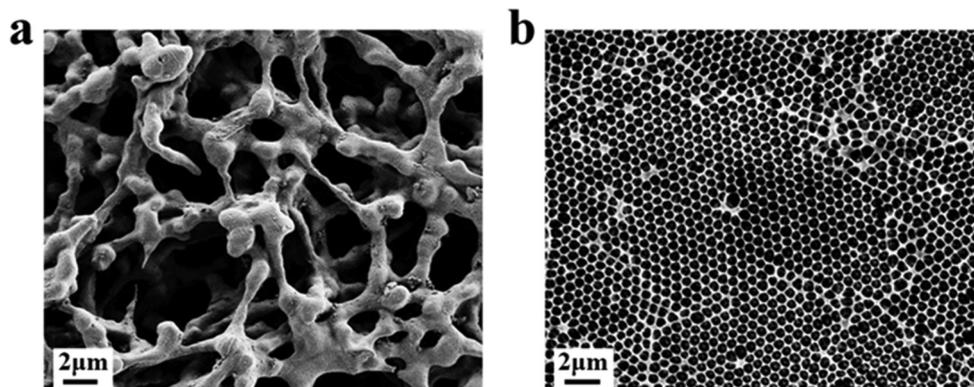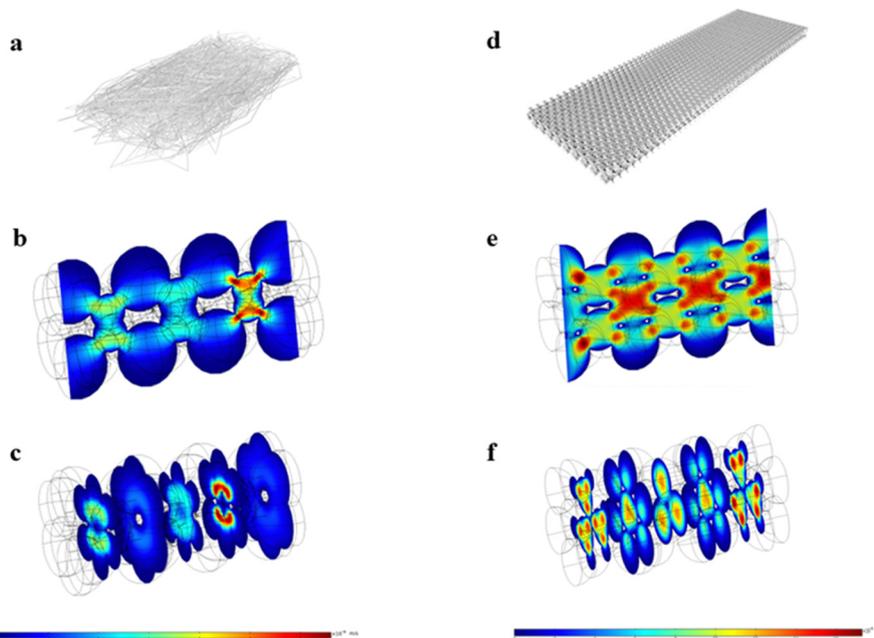

Fig. 7 SEM images of nanostructured and conventional T lines. (a) Conventional T line; (b) nanostructured T line.
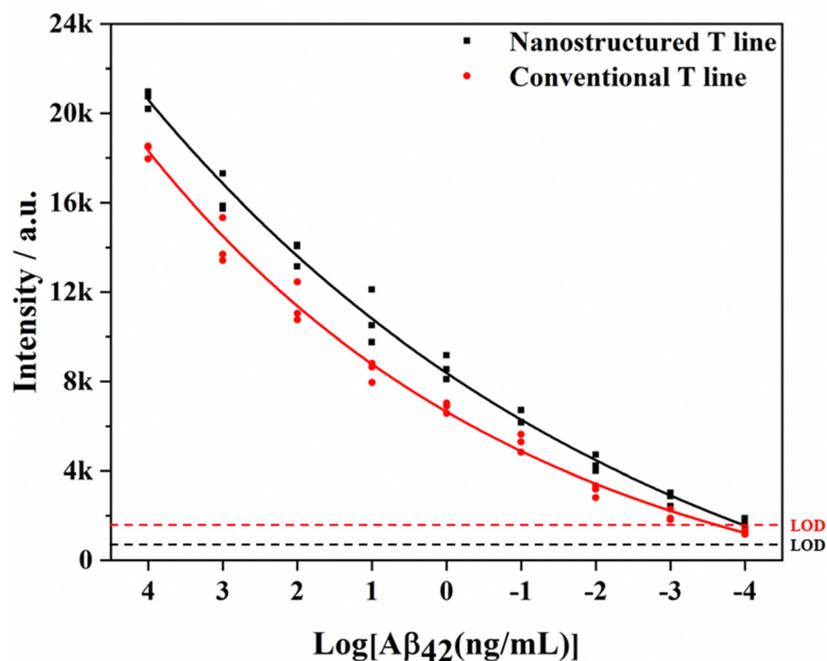
Fig. 8 (a) Schematic of conventional T line. (b) and (c) longitudinal-section and cross-section simulation results of fluid velocity in the conventional T line. (d) Schematic of the nanostructured T line. (e) and (f) Longitudinal-section and cross-section simulation results of fluid velocity in the nanostructured T line, respectively.

larger specific surface area is conducive to the immune reaction. However, the time required for reactant delivery needs to be limited to reduce reactant evaporation and improve detection efficiency. So, the trade-off between the reactant delivery and specific surface area motivates structural optimization for the entire NC membrane.[28]

Furthermore, the nanostructured T line is assembled into LFIA to detect different concentrations of $A\beta_{42}$. The comparison of test results and those of SERS-LFIA is shown in Fig. 9. For the same concentration of $A\beta_{42}$, SERS-LFIA with the nanostructured T line realizes higher Raman signals. In addition, the LODs of those SERS-LFIA for the detection of $A\beta_{42}$ are

Fig. 9 Comparison of Raman signals obtained by two SERS-LFIA detection of different concentrations of $A\beta_{42}$. Scatter plot of the nanostructured T line results for 3 measurements (black square) and scatter plot of the conventional T line results for 3 measurements (red circle).
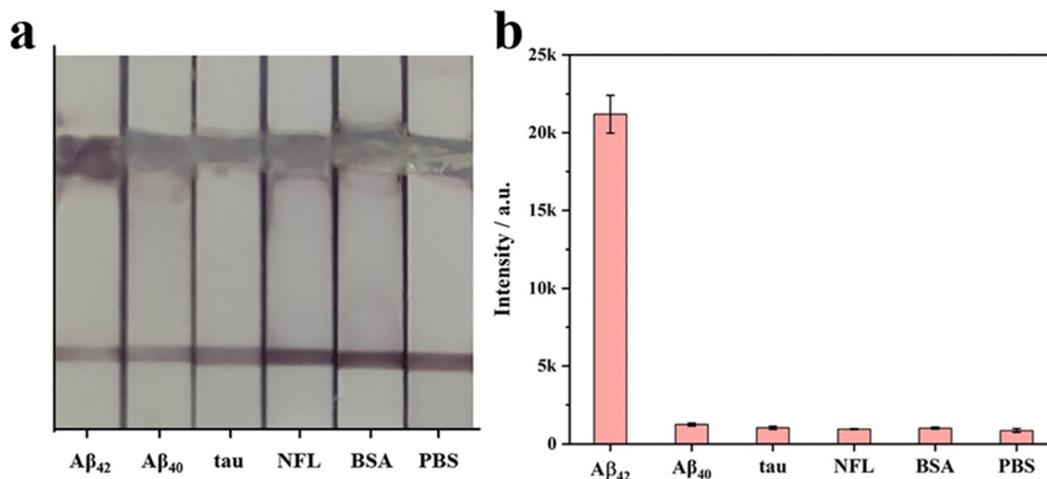
Fig. 10 Specificity evaluation of SERS-LFIA with the nanostructured T line. (a) The photograph of strips for detecting 10 μg mL^{-1} of different substances; (b) Raman signal intensity at 1079 cm^{-1} on the nanostructured T line. The error bars represent the average of three measurements.

calculated by the following equation, LOD = γ_{blank} + 3 × SD$_{blank}$, where γ_{blank} is the average signal intensity when the concentration is zero, and the SD$_{blank}$ represents the standard deviation. According to the standard curves (Fig. 11b),[19] the LODs of SERS-LFIA and SERS-LFIA with the nanostructured T line are 134.9 fg mL^{-1} and 15.3 fg mL^{-1}, respectively. The latter's LOD is about 10 times lower than the former's and exhibits better detection performance.

3.4. Detection of AD biomarkers

The specificity of SERS-LFIA with nanostructured T line is evaluated before AD biomarkers detection. Firstly, SERS-LFIA with a nanostructured T line is prepared for Aβ$_{42}$ detections. Then 10 μg mL^{-1} of Aβ$_{42}$, Aβ$_{40}$, tau, NFL, BSA, and PBS are added dropwise to the sample pad, respectively. The photograph of six test strips is shown in Fig. 10a, and all test strips' C lines are red, validating the test results. Only the test strips with the solution containing Aβ$_{42}$ appear red on the nanostructured T line, while the other test strips without Aβ$_{42}$ do not have a significant color change. The Raman signal on the nanostructured T line of each strip is also measured, and the signal intensity at

1079 cm^{-1} is compared. High Raman signals are detected on strips with the addition of Aβ$_{42}$ only, while Raman signals are hardly observed with other solutions, as shown in Fig. 10b, suggesting that the SERS-LFIA with the nanostructured T line exhibits high specificity, providing the foundation for subsequent multiplex quantitative detection.

Finally, SERS-LFIA with a nanostructured T line is used to detect Aβ$_{42}$ and Aβ$_{40}$ (Fig. 11). The linear dynamic range of Aβ$_{42}$ and Aβ$_{40}$ is 100 fg mL^{-1}–100 ng mL^{-1}, covering 6 orders of magnitude. In addition, the linear fitting coefficients (R^2) of Aβ$_{42}$ and Aβ$_{40}$ are 0.965 and 0.959, respectively, indicating a very high linear correlation. LOD is calculated based on the Raman signal intensity of the blank control group and its 3-fold standard deviation. The LODs of Aβ$_{42}$ and Aβ$_{40}$ are 15.3 and 16.8 fg mL^{-1}, respectively, about 10 times lower than that of conventional SERS-LFIA.[19]

The increase in sensitivity may be due to two aspects. On the one hand, the surface-to-volume of inverse opal nitrocellulose with an ordered structure is higher than the conventional one with a micron-sized irregular porous structure.[29,30] On the other hand, the nanoconfinement of pores as immunoreaction
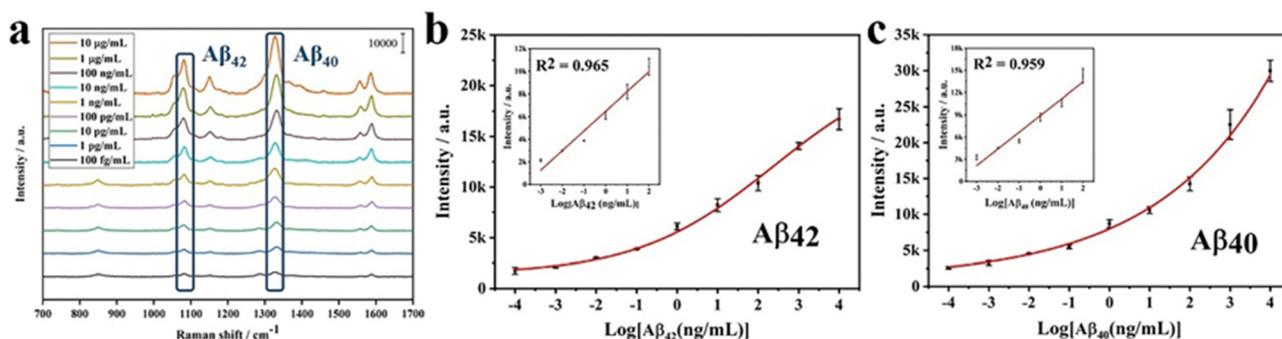

Fig. 11 SERS-LFIA with the nanostructured T line for AD biomarkers detection. (a) Raman spectra of SERS-LFIA with the nanostructured T line for Aβ$_{42}$ and Aβ$_{40}$ at different concentrations. (b) Standard curve of Raman signal intensities at 1079 cm^{-1} with the Aβ$_{42}$ concentration in figure (a). (c) Standard curve of Raman signal intensities at 1330 cm^{-1} with the Aβ$_{40}$ concentration in figure (a). The illustration is the linear fitting part of the standard curve.

nano-chambers also plays a key role, resembling the nanochannels array in vertical flow assays.[16,31]

4. Conclusions

A SERS-LFIA with a nanostructured T line is constructed and described. The concentration of NC solution and HF etching time are optimized during the preparation of inverse opal nitrocellulose. The optimal concentration of NC solution is 4%, and the optimal time for HF etching is 12 h. Inverse opal nitrocellulose with different pore diameters is successfully prepared by silica particles with different particle diameters. The best detection results are acquired with pore diameters of 350 nm. Finally, by detecting two AD biomarkers ($A\beta_{42}$ and $A\beta_{40}$), the LODs are 15.3 and 16.8 fg mL^{-1}, respectively, about 10 times lower than SERS-LFIA. This is the first time the nanostructured T line and LFIA combination are proposed, providing a new idea and theoretical basis to improve the LFIA sensitivity. Compared with the existing detection technologies for AD biomarkers detection, the method proposed has the advantages of strong specificity, high sensitivity, simple operation, low cost, multiple detection, and rapid detection, offering great potential for early diagnosis and AD monitoring.

Author contributions

Geng Zhu: methodology, investigation, data curation, writing – original draft. Yuanbao Zhan: methodology, investigation, data curation, writing – original draft. Yu Lu: methodology. Fei Zheng: software. Yu Wan: visualization. Bing Liu: data curation. Xi Yang: supervision. Yanhui Wan: methodology. Qingjiang Sun: methodology and resources. Jingjie Sha: formal analysis. Yan Huang: supervision, writing review and editing. Xiangwei Zhao: supervision, resources, writing review and editing. All authors read and approved the final manuscript.

Conflicts of interest

There are no conflicts to declare.

Acknowledgements

References

1 Z. Qu, K. Wang, G. Alfranca, J. M. de la Fuente and D. Cui, *Nanoscale Res. Lett.*, 2020, **15**, 10.

2 A. E. Cetin, A. F. Coskun, B. C. Galarreta, M. Huang, D. Herman, A. Ozcan and H. Altug, *Light: Sci. Appl.*, 2014, **3**, e122.

3 J. Liu, Z. Geng, Z. Fan, J. Liu and H. Chen, *Biosens. Bioelectron.*, 2019, **132**, 17–37.

4 W. Yan, K. Wang, H. Xu, X. Huo, Q. Jin and D. Cui, *Nanomicro Lett.*, 2019, **11**, 7.

5 M. Sajid, A.-N. Kawde and M. Daud, *J. Saudi Chem. Soc.*, 2015, **19**, 689–705.

6 E. Eltzov, S. Guttel, A. Low Yuen Kei, P. D. Sinawang, R. E. Ionescu and R. S. Marks, *Electroanalysis*, 2015, **27**, 2116–2130.

7 J. Tu, T. Wu, Q. Yu, J. Li, S. Zheng, K. Qi, G. Sun, R. Xiao and C. Wang, *J. Hazard. Mater.*, 2023, **448**, 130912.

8 C. Parolo, A. Sena-Torralba, J. F. Bergua, E. Calucho, C. Fuentes-Chust, L. Hu, L. Rivas, R. Alvarez-Diduk, E. P. Nguyen, S. Cinti, D. Quesada-Gonzalez and A. Merkoci, *Nat. Protoc.*, 2020, **15**, 3788–3816.

9 D. Zhang, L. Huang, B. Liu, H. Ni, L. Sun, E. Su, H. Chen, Z. Gu and X. Zhao, *Biosens. Bioelectron.*, 2018, **106**, 204–211.

10 L. Wang, X. Wang, L. Cheng, S. Ding, G. Wang, J. Choo and L. Chen, *Biosens. Bioelectron.*, 2021, **189**, 113360.

11 M. Lu, Y. Joung, C. S. Jeon, S. Kim, D. Yong, H. Jang, S. H. Pyun, T. Kang and J. Choo, *Nano Converg.*, 2022, **9**, 39.

12 O. J. Clarke, B. L. Goodall, H. P. Hui, N. Vats and C. L. Brosseau, *Anal. Chem.*, 2017, **89**, 1405–1410.

13 W. Guo, J. Hansson and W. van der Wijngaart, *Anal. Chem.*, 2020, **92**, 6194–6199.

14 J. Hansson, H. Yasuga, T. Haraldsson and W. van der Wijngaart, *Lab Chip*, 2016, **16**, 298–304.

15 W. Guo, L. Vilaplana, J. Hansson, M. P. Marco and W. van der Wijngaart, *Biosens. Bioelectron.*, 2020, **163**, 112279.

16 R. Chen, X. Du, Y. Cui, X. Zhang, Q. Ge, J. Dong and X. Zhao, *Small*, 2020, **16**, e2002801.

17 B. Gao, H. Liu and Z. Gu, *Anal. Chem.*, 2016, **88**, 5424–5429.

18 J. Chi, B. Ma, X. Dong, B. Gao, A. Elbaz, H. Liu and Z. Gu, *Analyst*, 2018, **143**, 4559–4565.

19 Y. Zhan, R. Fei, Y. Lu, Y. Wan, X. Wu, J. Dong, D. Meng, Q. Ge and X. Zhao, *Analyst*, 2022, **147**, 4124–4131.

20 B. Gao, X. Wang, T. Li, Z. Feng, C. Wang and Z. Gu, *Adv. Mater. Technol.*, 2019, **4**, 1800392.

21 L. Zheng, X. Dong, J. Chi, M. Sun, C. Zhao and H. Liu, *New J. Chem.*, 2019, **43**, 4808–4814.

22 B. Gao, Y. Yang, J. Liao, B. He and H. Liu, *Lab Chip*, 2019, **19**, 3602–3608.

23 Z. Gu, A. Fujishima and O. Sato, *Chem. Mater.*, 2002, **14**, 760–765.

24 J. Hou, M. Li and Y. Song, *Angew. Chem., Int. Ed.*, 2018, **57**, 2544–2553.

25 J. Chi, B. Gao, M. Sun, F. Zhang, E. Su, H. Liu and Z. Gu, *Anal. Chem.*, 2017, **89**, 7727–7733.

26 X. Zhao, J. Xue, Z. Mu, Y. Huang, M. Lu and Z. Gu, *Biosens. Bioelectron.*, 2015, **72**, 268–274.

27 C. L. A. Berli and P. A. Kler, *Microfluid. Nanofluid.*, 2016, **20**, 104.

28 P. Jia, Z. Li, X. Wang, F. Xu, M. You and S. Feng, *Int. Commun. Heat Mass Transfer*, 2023, **143**, 106729.

29 Z. Mu, X. Zhao, Y. Huang, M. Lu and Z. Gu, *Small*, 2015, **11**, 6036–6043.

30 J. Chi, C. Shao, X. Du, H. Liu and Z. Gu, *ACS Appl. Mater. Interfaces*, 2018, **10**, 39144–39150.

31 D. B. Gornowich and G. J. Blanchard, *J. Phys. Chem. C*, 2012, **116**, 12165–12171.